ORNL/SPR-2025/4088
M3LW-25OR0402053

Light Water Reactor Sustainability Program

Mass Spectrometry Characterization of High Fluence Baffle-Former Bolts Retrieved from a Westinghouse PWR

Timothy G. Lach
Gabriel Parker
Xiao-Ying Yu
Xiang (Frank) Chen

August 2025

U.S. Department of Energy
Office of Nuclear Energy

DISCLAIMER

This information was prepared as an account of work sponsored by an agency of the U.S. Government. Neither the U.S. Government nor any agency thereof, nor any of their employees, makes any warranty, expressed or implied, or assumes any legal liability or responsibility for the accuracy, completeness, or usefulness, of any information, apparatus, product, or process disclosed, or represents that its use would not infringe privately owned rights. References herein to any specific commercial product, process, or service by trade name, trademark, manufacturer, or otherwise, does not necessarily constitute or imply its endorsement, recommendation, or favoring by the U.S. Government or any agency thereof. The views and opinions of authors expressed herein do not necessarily state or reflect those of the U.S. Government or any agency thereof.

ORNL/SPR-2025/4088
M3LW-25OR0402053

Light Water Reactor Sustainability (LWRS) Program
Materials Research Pathway

MASS SPECTROMETRY CHARACTERIZATION OF HIGH FLUENCE BAFFLE-FORMER BOLTS RETRIEVED FROM A WESTINGHOUSE PWR

Timothy G. Lach, Gabriel Parker, Xiao-Ying Yu, Xiang (Frank) Chen

Materials Science and Technology Division
Oak Ridge National Laboratory

August 2025

Prepared by
OAK RIDGE NATIONAL LABORATORY
Oak Ridge, TN 37831-6136
managed by
UT-BATTELLE LLC
for the
US DEPARTMENT OF ENERGY
under contract DE-AC05-00OR22725

CONTENTS

LIST OF FIGURES

LIST OF TABLES

ACKNOWLEDGMENT

This research was sponsored by the U.S. Department of Energy, Office of Nuclear Energy, Light Water Reactor Sustainability Program, Materials Research Pathway, under contract DE-AC05-00OR22725 with UT-Battelle, LLC/Oak Ridge National Laboratory (ORNL).

The authors extend their appreciation to Clay Morris, Jerid Metcalf, and other colleagues at Irradiated Materials Examination and Testing Facility (IMET) at ORNL for their support of sample processing during the hot cell sample retrieval. In addition, we would like to thank Patricia Tedder and Kyle Everett at the Low Activation Materials Development and Analysis (LAMDA) laboratory at ORNL for receiving, cleaning, inventorying, and polishing the irradiated samples. We would also like to thank Dr. Maxim Gussev for his thoughtful discussion and characterization for prior results within this task. Lastly, we would like to thank the late Mike Burke formerly with Electrical Power Research Institute who was involved in the bolt harvesting and characterization planning and led the sample preparation, machining, and shipping when he was working at Westinghouse Electric Company. We would like to acknowledge the Center for Nanophase Materials Sciences and the LAMDA lab at ORNL for enabling the FIB/SEM, TEM, APT, and ToF-SIMS characterization.

EXECUTIVE SUMMARY

Baffle-former bolts (BFBs) are subjected to significant mechanical stress and neutron irradiation from the reactor core during the plant operation. Over the long operation period, these conditions lead to potential degradation and reduced load-carrying capacity of the bolts, and life extension of existing pressurized water reactors (PWRs) would only cause more damage to the bolt material. To this end, the Light Water Reactor Sustainability (LWRS) Program Materials Research Pathway (MRP) successfully harvested two high fluence BFBs from a Westinghouse two-loop downflow type PWR in 2016. In the same year, the two BFBs were received at the Westinghouse Churchill facility for inspection and specimen fabrication. The fabrication was completed in 2017 with specimens shipped to Oak Ridge National Laboratory (ORNL) for further testing. The objective of this project is to provide information that is integral to evaluating high fluence microstructure and properties as a benchmark of international models developed for predicting radiation-induced swelling, segregation, precipitation, mechanical property degradation, and susceptibility to irradiation-assisted stress corrosion cracking (IASCC).

In this report, we present our latest study in FY25 on microstructural and mass spectrum characterizations of the gradients of transmutation gas concentration and cavity density and size along the length of the high dose BFBs. The main findings are summarized as follows:

1. The cavity size distribution was quantified along the length of the high dose bolt #4412 using under-focus transmission electron microscopy. The bolt head section (CS) had a high number density of nanocavities with an average radius of 1.9 nm and a number density of 4.4×10^{22} m^{-3}. The bolt mid-shank (MS) and bolt thread (BS) sections had larger cavities and a lower number density, with the BS section having a clear bimodal distribution. The MS section had an average cavity radius of 3.4 nm and a number density of 4.7×10^{21} m^{-3}. The BS section had an average cavity radius of 4.1 nm and a number density of 5.4×10^{21} m^{-3}, but the distribution of cavities was centered around radii of 2.5 nm and 5 nm. This gradient is consistent with the bolt head having less hydrogen and being at a lower temperature than the bolt shank and thread.
2. Hydrogen isotopes protium and deuterium were detected by ToF-SIMS in the high dose BFB #4412. The results did not show a clear statistically significant difference between sections of the bolt. However, the data were collected on relatively small liftouts and so further analysis by different ToF-SIMS techniques and on larger samples should help identify any gradients in the hydrogen and helium isotope concentrations. The presence of non-background hydrogen was also confirmed by APT, as a peak at 3 Da was also identified in every sample from both high-dose and low-dose bolts – a peak that is not present in unirradiated stainless steels.
3. Lessons were learned on the difficulty of measuring hydrogen (and helium) isotopes. The FIB/SEM work requires precision and production of large samples for ToF-SIMS, in order to remove artefacts from sample analysis – due to hydrocarbon interference. In addition, changing the data collection method such as through the CsM^+ is needed to collect concentration data for inert gases such as helium. Detection of hydrogen isotopes by APT is also possible; however, sample preparation and transfer need to be conducted at cryogenic temperatures in ultra-high vacuum to limit hydrogen mobility. These lessons will be applied to future work on these and other materials, including the bolt head/shank surface oxide.

1. INTRODUCTION

As one of the pressurized water reactor (PWR) internal components, baffle-former bolts (BFBs) are subjected to significant mechanical stress and neutron irradiation from the reactor core during the plant operation. Over the long operation period, these conditions lead to potential degradation and reduced load-carrying capacity of the bolts, and life extension of existing PWRs would only cause more damage to the bolt material. Indeed, the BFB has been a particular concern for the nuclear industry since the first observation of failed bolts following the investigation of flow-induced vibration of fuel rods in elements on the core periphery observed in French 900 MW plants in the 1980s [1]. In the United States, the first degraded BFBs were observed in 1999. In support of evaluating long-term operation performance of materials used in core internal components, the Materials Research Pathway (MRP) under the U.S. Department of Energy (DOE), Office of Nuclear Energy, Light Water Reactor Sustainability (LWRS) Program pursued the retrieval of aged structural components for the study of the microstructure, mechanical, and corrosion-related properties. To this end, the MRP successfully harvested two high fluence BFBs from a Westinghouse two-loop downflow type PWR in 2016. In the same year, the two BFBs were received at the Westinghouse Churchill facility for inspection and specimen fabrication. The fabrication was completed in 2017 with specimens shipped to Oak Ridge National Laboratory (ORNL) for further testing.

In this report, we present our latest study in FY25 on microstructural and mass spectrum characterizations of the transmutation products and gas-filled bubbles of the high dose BFB. The objective of this project is to provide information that is integral to evaluating high fluence microstructure and properties as a benchmark of international models developed for predicting radiation-induced swelling, segregation, precipitation, and mechanical property degradation. This project task performed characterizations in FY19 [2], FY22 [3], FY23 [4], and FY24 [5] which focused on electron microscopy and atom probe tomography (APT)-based microstructural characterizations and microhardness testing for both harvested BFBs and the surface oxide structure and grain boundary attack. Fracture toughness and fatigue crack growth rate testing results of both BFBs have also been published in the FY21 milestone report [6] for this project. This previous work from this task filled the knowledge gaps for radiation-induced microstructural evolution and mechanical property evolution. The results showed that radiation-induced precipitation, dislocation loop formation, and nanocavity evolution in the two BFBs was highly complex, with the volume fraction and size of Ni/Si and Cu-rich precipitates, dislocation loops, and nanocavities depending strongly on the radiation temperature/dose. The bolt thread end in each bolt had larger precipitates, loops, and nanocavities than the bolt head end. Specifically for clustering, comparing the two bolts, clustering was essentially the same for both bolts in the CS or bolt head section, but Ni/Si clustering was much higher in the BS or bolt thread section in the high dose bolt #4412 than in the lower dose bolt #4416. The results from FY24 presented on the study of in-service IASCC via scanning electron microscopy (SEM)-electron backscatter diffraction (EBSD) and energy dispersive X-ray spectroscopy (EDS) imaging and mapping, transmission electron microscopy (TEM), and analytical scanning TEM (STEM) at the intersection of the bolt head and bolt shank in the higher dose bolt which was exposed to primary coolant water. IASCC requires an environmentally-susceptible material, a corrosive environment, radiation, and mechanical stress. The bolt head/shank intersection in PWR BFBs meets all four requirements but with aspects that were not observed in laboratory experiments previously [5, 7, 8].

In this FY25 report, we delve deeper into the effects of the irradiation environment, specifically transmutation effects on radiation hardening and IASCC. We sought to compare the gradients observed in TEM of cavity size and density along the length of each bolt with the measured hydrogen isotope concentrations of each bolt section. Time-of-flight secondary ion mass spectrometry (ToF-SIMS) was used to characterize the BFB mid-shank and collar slice sections. High lateral resolution surface spectra and high spatial resolution imaging were captured in both positive and negative polarity providing information regarding hydrogen and deuterium distributions as well as possible steel transmutation products and isotope distributions.

2. EXPERIMENTAL METHODS

2.1 Materials

The two harvested BFBs had the highest fluence among bolts withdrawn from service in 2011. Both bolts showed no indication of cracking during the ultrasonic inspection and in visual inspection following removal from service. However, the bolts required a lower torque for removal from the baffle structure than the original torque specified during installation. Figure 1 shows images of the bolt heads of two retrieved BFBs; no indication of surface cracking was observed in the transition region between the shaft and head, although some surface debris scale flaked off from the bolt body. The shiny gray portion of the bolt head was due to electric discharge machining (EDM) when the bolts were removed from the baffle wall. However, both bolts do still have some of the original surface that was exposed to coolant water where the bolt head intersects with the bolt shank, as circled in Figure 1b. The ID number for the bolts follows a 4-digit code with the first number being the quadrant location in the reactor, then the associated baffle plate number, the column location of the bolt associated with the particular baffle plate number, and finally the former plate location where the bolt originated. The compositions of the bolts, as determined by APT in both atomic percent (at%) and weight percent (wt%), are presented in Table 1 [4]. These bolts are within the specifications for type 316-SS excepting slightly elevated Cr content, but this could be due to local variations.

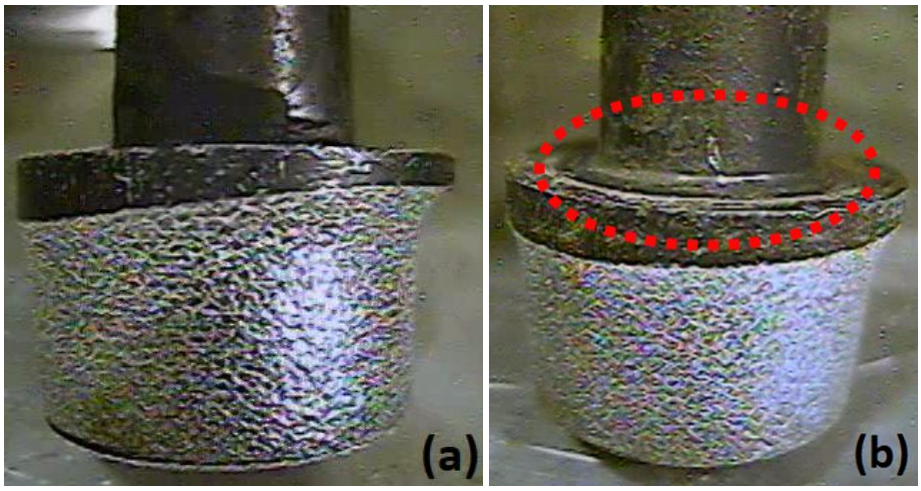

Figure 1: Images of bolt heads for bolt #4412 in (a) and bolt #4416 in (b). Surface of bolt at bolt head/shank intersection (circled) was exposed to primary water and is still intact [9].

Table 1: Average compositions of bolt 4412 and 4416 from APT reconstructions for each bolt [10] in comparison with material specification (wt%) for 316 SS

	BFB-4412		BFB-4416		316-SS Spec
Element	at%	wt%	at%	wt%	wt%
Fe	64.19	64.62	64.56	64.96	Bal.
Ni	11.55	12.22	11.39	12.04	10.00-14.00
Cr	19.32	18.11	19.36	18.14	16.00-18.00
Mn	1.62	1.60	1.67	1.65	2.00 max
Mo	1.18	2.04	1.18	2.04	2.00-3.00
Si	1.24	0.63	1.15	0.58	1.00 max
C	0.20	0.043	0.19	0.040	0.08 max

P	0.024	0.013	0.027	0.015	0.040 max
Cu	0.26	0.29	0.25	0.28	0.75 max

Table 2 provides information on the range of fluences and estimated displacement damage along the length of the two bolts. The displacement damage values for the two bolts range from 15 to 41 displacements per atom (dpa) assuming a fluence to dpa conversion value of 6.7×10^{20} n/cm^2, E > 1 MeV per dpa [11]. Other important information for the two retrieved bolts not available to this report includes the irradiation temperature profile, irradiation flux, and thermomechanical stress state. These require more complicated modeling and calculation and can vary within each power cycle and from cycle to cycle. For instance, calculations from Point Beach Unit 2 [12], which is another Westinghouse two-loop type PWR, showed that the irradiation temperature and flux for a BFB from a region next to the bolt 4416 studied in this work varied in the range of 323-344 °C and 7.5×10^{12}-1.8×10^{13} n/cm^2-sec (E > 1 MeV) along the length of the bolt, respectively. Similarly, a baffle-former bolt removed from the Tihange 1 PWR showed a variation in irradiation temperature of about 23 °C (320-343 °C) along the bolt and a damage dose that was 2.6X higher in the bolt head (19.5 dpa) than the bolt thread (7.5 dpa) [13]. Therefore, the value for a detailed calculation on irradiation temperature and flux of BFBs may be limited due to the large variation of those parameters during the lifetime of a BFB. It should be noted that Point Beach Unit 2 was originally a Westinghouse two-loop downflow type PWR but was converted to upflow in 1986 [12].

Table 2: Fluence and estimated displacement damage distributions for two retrieved BFBs

Bolt #	Fluence (10^{22} n/cm^2, E > 1 MeV)/Estimated dpa		
	Head	Mid-shank	Mid-thread
4412	2.78/41	2.27/34	1.46/22
4416	1.91/29	1.56/23	1.00/15

The specimen machining plan is shown in Figure 2. For each BFB, four bend bar specimens and seven thin slice specimens were machined. The bend bar specimens were used in the fracture toughness and fatigue crack growth rate studies, whereas the thin slice specimens are planned for subscale tensile and microstructural analyses. Specimens were machined from different fluence regions of each bolt, allowing for studies of the effect of fluence on the microstructural and mechanical properties of BFBs. Three thin slice specimens were machined from the high-stress concentration region, i.e., the transition between the bolt head and shank, of each bolt to allow for further investigation of possible crack initiation sites.

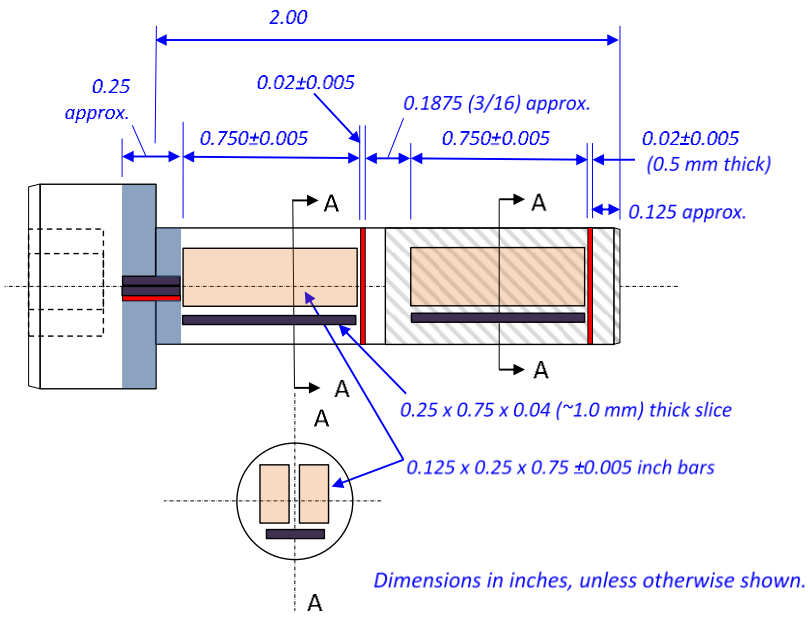

Figure 2: Machining diagram for the BFBs showing the color-coded sample types (red: 0.5 mm slices, black: 1.0 mm slices, light orange: bend bars, and light blue: remaining collar materials) [14]

2.2 Characterization methods

2.2.1 Electron microscopy

Liftouts for transmission electron microscopy (TEM) and time-of-flight – secondary ion mass spectrometry (ToF-SIMS) from each section of the bolt were made using a Thermo Fisher Versa3D focused ion beam (FIB)/SEM. The TEM sample preparation followed the procedures of initial trenching, cutting, and thinning to 200 nm with 30 keV Ga^+ beam, thinning to ~100 nm with the ion beam energy reduced to 8 keV and 5 keV and finally a clean polish at 2 keV. Before loading into the TEM, samples were cleaned with a Fischione 1020 Nanomill for 10 minutes on each side using 900 eV Ar^+ ions. Microstructural characterization was performed with transmission Kikuchi diffraction (tKD) using the Tescan Mira3 SEM and TEM/ scanning TEM (STEM) with energy-dispersive spectroscopy (EDS)-based mapping using a Thermo Fisher Talos F200X TEM/STEM equipped with a quadrupole SuperX Si-drift detector EDS system, a high resolution Gatan Ceta camera, and bright field (BF) and three annular dark field (ADF) detectors – low angle ADF (LAADF), medium angle ADF (MAADF), and high angle ADF (HAADF). To detect small nanocavities, Fresnel contrast imaging was used via under-focus and over-focus BF TEM.

The ToF-SIMS sample preparation in the FIB/SEM followed a two-step process, with the first step being similar to the TEM preparation. The liftouts were made approximately 10 µm in depth, 10 µm in width, and a thickness of 1 µm. The liftouts were attached in a “flag-pole” fashion to standard Cu FIB half grids. The FIB/SEM chamber was then opened and the grids were put on their side. The Omniprobe needle was reattached to the liftout, and the liftout was then cut away from the grid. The liftout was moved over and attached flat to a pure Si wafer. Snapshots of this process are shown in Figure 3.

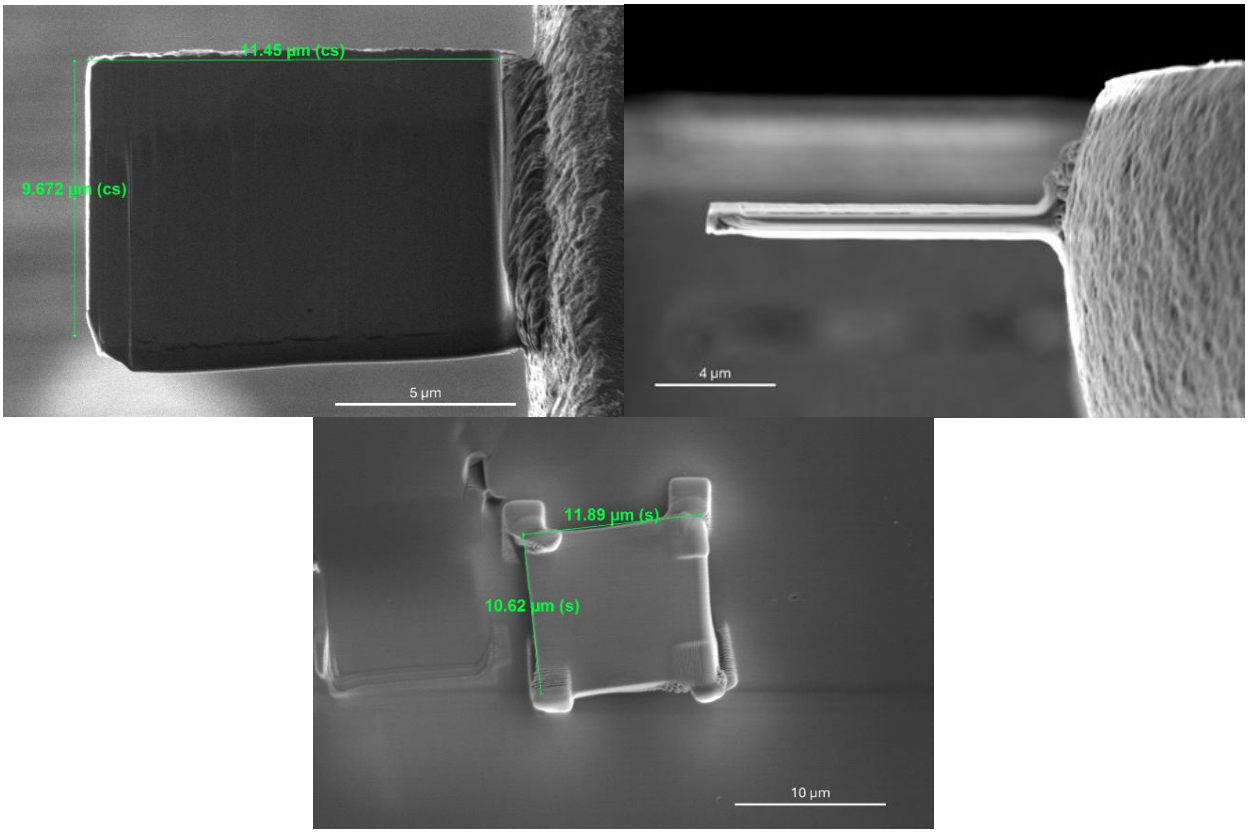

Figure 3: FIB/SEM liftout procedure for ToF-SIMS. A liftout, similar to a TEM liftout, is attached to a Cu grid as shown in (a, b) and thinned to under 1 µm. The grid is then laid on its side, where the liftout is detached and then attached to pure Si wafer as shown in (c).

2.2.2 Time-of-Flight – Secondary Ion Mass Spectrometry

Time-of-flight secondary ion mass spectrometry (ToF-SIMS) utilized a 30 keV Bi^{3+} primary ion beam to capture surface spectra data and high-resolution imaging data. A schematic for the fundamentals of ToF-SIMS is shown in Figure 4 [15]. During surface spectra collection the IONTOF ToF-SIMS V-NCS (IONTOF GmBH, Germany) Bi^{3+} primary ion beam had an ion current of 30.8 nA and a 2 keV O_2 sputter ion beam, used to clean the surface, had an ion current of 173.69 nA. The cycle time for collection was 100 µs. Spectra were collected in positive and negative polarity using a 21 eV electron flood gun for charge compensation. Surface spectra were collected in 100×100 µm and 50×50 µm analysis areas. The pixel resolution was 256×256 and 512×512, respectively. The total number of scans were set to 60 for each collection. Five replicate measurements were captured for reproducibility.

High resolution imaging mode using the ToF-SIMS was collected in positive and negative polarity. The cycle time was 100 µs. The primary ion beam was Bi^{3+} and had an ion current of 0.463 nA. A 21 eV electron flood gun was used for charge compensation. Images were collected in 100×100 µm and 20×20 µm areas. Image resolution was captured in 256×256 and 512×512 pixels. The total number of scans were set to 60 for each collection. The ToF-SIMS secondary electron (SE) detector was used to collect secondary electron images of the sample surface. ToF-SIMS SE images were collected in positive polarity. SE images were collected in 100×100 µm and 20×20 µm areas. SE image resolution was captured in 512×512 pixels.

ToF-SIMS spectra and images were analyzed using SurfaceLab 7.3 software (IONTOF GmBH, Germany). Spectra were calibrated in the negative polarity using (m/z^-) H^- (1.0084), C_2^- (24.0001), O_2^- (31.9904), and FeO_2^- (87.9253) and in the positive polarity using (m/z^+) H^+ (1.0072), Al^+ (26.9801), Cr^+ (51.9400), Fe^+ (55.9349), and Ni^+ (57.9348). Steel-316, 4412 MS and 4412 CS samples had mass resolution

values of between 8000 – 11000 at FeO_2^- respectively in negative polarity. Mass resolution in positive polarity values were 7000 – 8500 at Cr^+ respectively. Calibrated ToF-SIMS spectra data was exported to ASCII files and plotted using OriginPro software (OriginLab, Northampton, Massachusetts). The "search compounds" function was used to identify steel fragments and isotopes. Best matches based on relative mass accuracy and supported by literature and database records were identified and recorded. Peaks with a deviation of less than 100 ppm are included in the findings.

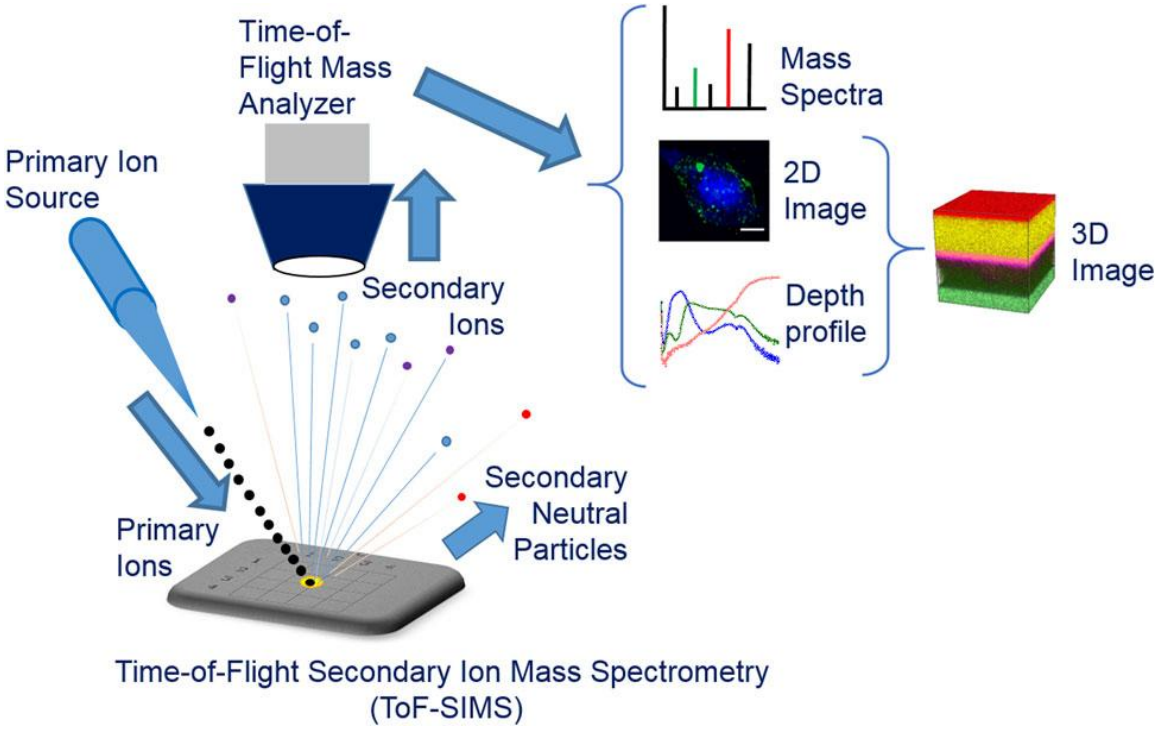

Figure 4: Time-of-flight secondary ion mass spectrometry overview showing the capabilities of mass spectra collection, 2D image collection, depth profile collection, and 3D image reconstruction using 2D image stacks produced via depth profiling. Adapted from ref [15].

3. RESULTS AND DISCUSSION

3.1 Characterization of cavity structure along length of bolt

Figure 5 shows under-focus TEM images of the CS, MS, and BS sections of the BFB #4412, as well as a histogram for the cavity sizes for each section of the bolt. The BS and MS sections have much larger cavities, while the CS section has a higher number density of small cavities. The BS section has a clear bimodal distribution of large cavities with a radius of ~5 nm and small cavities with a ~2 nm radius. The average cavity radius in the BS section is 4.1 nm with a number density of 5.4×10^{21} m^{-3}. The MS section is similar to the BS section but the cavities are slightly smaller with a less pronounced bimodal distribution, though it is still there with larger cavities centered at a radius of ~4.5 nm and smaller cavities at a radius of ~3 nm. The average cavity radius in the MS section is 3.4 nm with a number density of 4.7×10^{21} m^{-3}. The CS section has about an order of magnitude higher number density but of much smaller cavities with a radius centered at ~2 nm. The average cavity radius in the CS section is 1.9 nm with a number density of 4.4×10^{22} m^{-3}. The larger cavities are indicative of gradients in temperature, strain, fast/thermal neutron energy, and potentially hydrogen concentration from transmutation or exposure to PWR water [16], with each of these being higher in the bolt thread section (BS) than in the bolt head section (CS). Vacancies, along with an abundance of hydrogen, are much more mobile due to thermal and strain gradients where they can gather into vacancy clusters and grow into large cavities that could be gas-filled. This is consistent with what was seen in the BFB #4416 [2] and with analysis of a baffle-former bolt retrieved from the Tihange 1 reactor [13]. The large amount of hydrogen together with transmutant helium may together stabilize cavities and lead to cavity growth. With this gradient in cavity size, which could have a significant impact on hardening and in turn on IASCC susceptibility, it is important to quantify the amount of transmutant hydrogen and helium species inside the bolts. Thus, we used mass spectrometry techniques such as ToF-SIMS and APT.

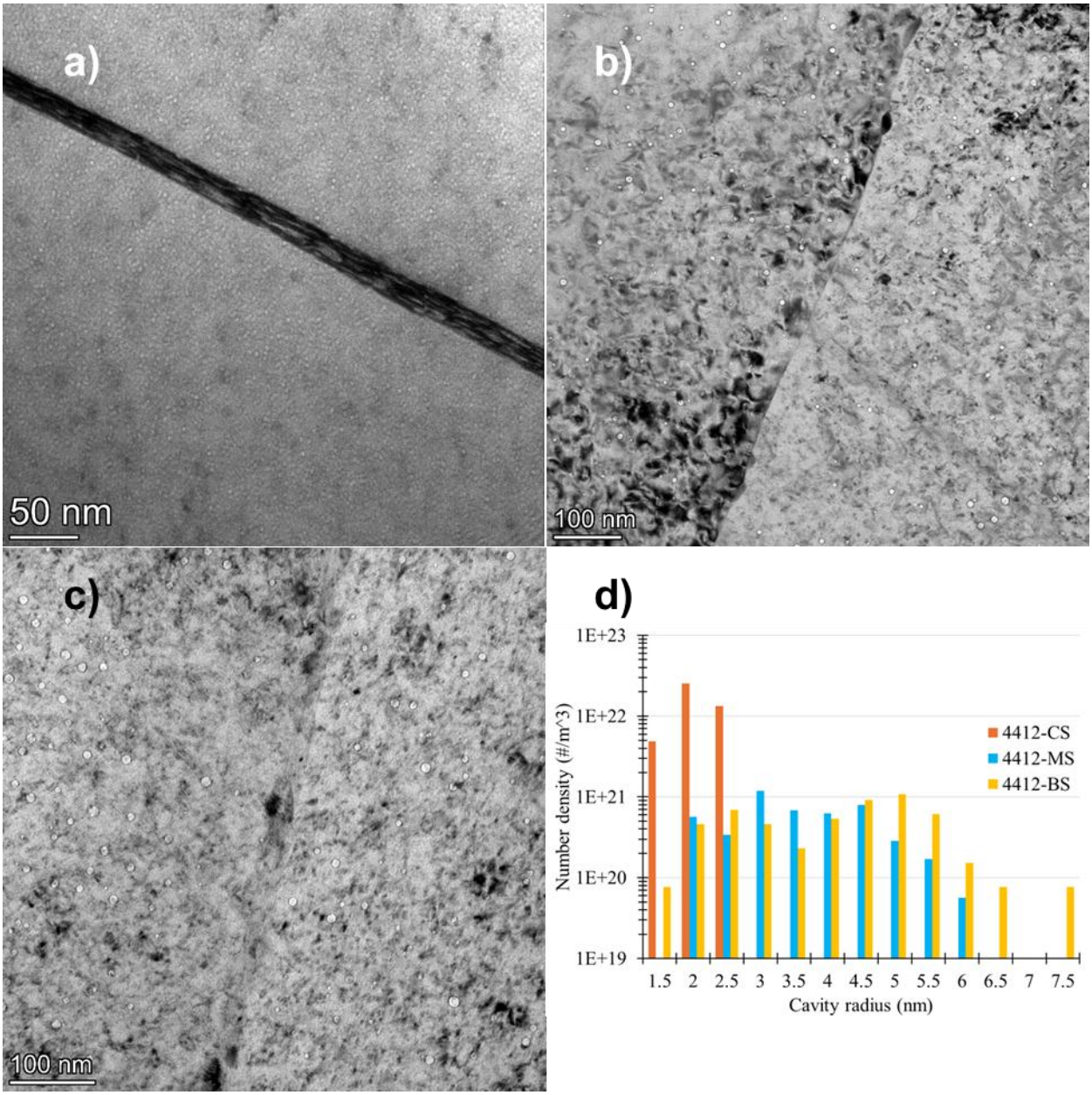

Figure 5: Underfocused BF-TEM images of (a) 4412-CS, (b) 4412-MS, and (c) 4412-BS sections of the bolt. Cavities are observed in each section though their sizes vary significantly, as depicted in the cavity radius histogram in (d).

3.2 Isotopic measurements using Time-of-Flight – Secondary Ion Mass Spectrometry

High resolution spectra were captured on the BFB collar slice (4412 CS), mid-shank (4412 MS) and steel-316 control for comparison of spectra differences in transmutation product and isotope analysis. Spectra collection shows values up to m/z^+ 250, highlighting steel molecular components such as Ti, Cr, V, Mn, Fe, Ni, Co, and Cu. Hydrocarbons are also observed within the spectra. The spectra were collected up to m/z^+ 250, and Figure 6 highlights the region of m/z^+ 45-65. Values found within the high-resolution spectra collection allow for determination of spatial distribution within the high-resolution imaging detection. While positive polarity did not identify deuterium, negative polarity shows protium and deuterium within the spectrum. Low deuterium counts may be attributed to sample un-evenness or trapped

deuterium in the sample. Figure 7 shows the spectra for ^{1}H and ^{2}H observed using ToF-SIMS high-resolution spectra collection. Identification of ^{1}H, ^{2}H, ^{3}H, and He are possible using ToF-SIMS depth profiling using the Cs to provide a CsM^{+} identification is needed. CsM^{+} is a SIMS technique utilizing the bombardment of Cs to cause adduct formation of analyte, M, to appear in the spectra. Not shown in Figure 6 is the large peak at a m/z^{+} of 69, which is Ga from the FIB/SEM. Using depth profiling will also eliminate this preparation artefact, as the damaged depth of the Ga-ion may also impact the local composition.

Positive spectra collection highlighting steel components observed within m/z^{+} 45-65 are overlapped and compared against one another in Figure 8. The steel-316 sample was shown to have the highest intensity values for Ti, Cr, Fe, Ni, and Co. However, the 4412 MS sample using a selected region of interest capturing the BFB showed higher intensity values for V, Mn, and Cu. These values, especially for Mn, are well outside of what was observed by APT [4]; thus, there are artefacts like sample size and geometry that must be considered. The collar slice did not show high intensity values. Ti and V were not observed in the 4412 CS sample and only trace amounts of Co and Cu were observed. High resolution imaging provides spatial information of the BFB showing the spatial distribution of steel components. Figure 9 provides the high-resolution images captured via ToF-SIMS. Silicon is observed at the edges of the BFBs in both 4412 MS and 4412 CS. It is noted that Ga covers the surface of the sample which could be the reason for the low counts observed. Transmutation products like V and Ti can possibly originate from neutron-induced reactions of ^{50}Cr and ^{52}Cr. Further work is required on larger liftouts along with depth profiling. These together should help improve the statistical counts and remove artefacts such as the Pt-C 'weld' and Ga-implantation from the FIB/SEM.

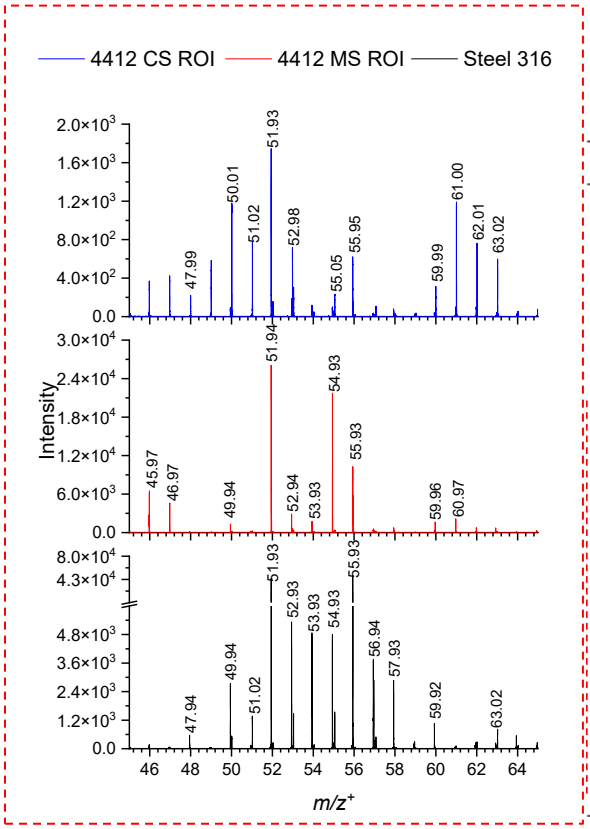

			316 Steel Control	4412 MS ROI	4412 CS ROI
Center Mass (u)	*Ion Mass (u)*	*Assignment*	*Mass Deviation (ppm)*	*Mass Deviation (ppm)*	*Mass Deviation (ppm)*
1.00726	1.007276	H^+	-16.3189	-20.385	-68.3292
2.015038	2.015101	H_2^+	-31.5219	-28.4255	-67.5978
3.022809	3.022927	H_3^+	--	--	-39.0326
22.98908	22.98922	Na^+	-6.29595	1.163125	10.07545
26.98108	26.98099	Al^+	3.37735	14.23987	-13.1548
27.97638	27.97638	Si^+	0.053542	120.3699	4.871103
38.96488	38.96316	K^+	44.06409	10.06964	40.82558
45.95155	45.95208	$^{46}Ti^+$	-11.6457	--	--
46.95103	46.95122	$^{47}Ti^+$	-3.86508	--	--
47.94755	47.9474	Ti^+	3.235227	--	--
48.94594	48.94732	$^{49}Ti^+$	-28.2736	--	--
49.94487	49.9455	$^{50}Cr^+$	-12.7414	13.92663	-14.2791
50.9452	50.94342	V^+	35.10221	32.07958	--
51.94029	51.93996	Cr^+	6.353252	18.29216	-0.79936
52.93971	52.94011	$^{53}Cr^+$	-7.47507	1.482642	1.233387
53.93813	53.93907	$^{54}Fe^+$	-17.3754	-3.22722	-13.3229
54.9364	54.9375	Mn^+	-20.1222	4.962174	-11.8764
55.93494	55.93439	Fe^+	9.767436	13.29551	-3.15057
56.93912	56.93485	$^{57}Fe^+$	74.9985	38.18705	--
57.93346	57.9348	Ni^+	-23.1083	2.40919	-10.3521
58.93179	58.93265	Co^+	-14.5716	9.827813	--
59.92907	59.93024	$^{60}Ni^+$	-19.6336	9.95127	-16.8253
61.92661	61.9278	$^{62}Ni^+$	-19.287	--	--
62.92763	62.92905	Cu^+	-22.6414	3.931795	--
64.92565	64.92725	$^{65}Cu^+$	-24.5709	4.913009	--
97.90544	97.90486	Mo^+	53.5679	5.921972	29.56423

Figure 6: ROI analysis provides cleaner spectra, allowing for peak determination in the high spatial resolution imaging mode.

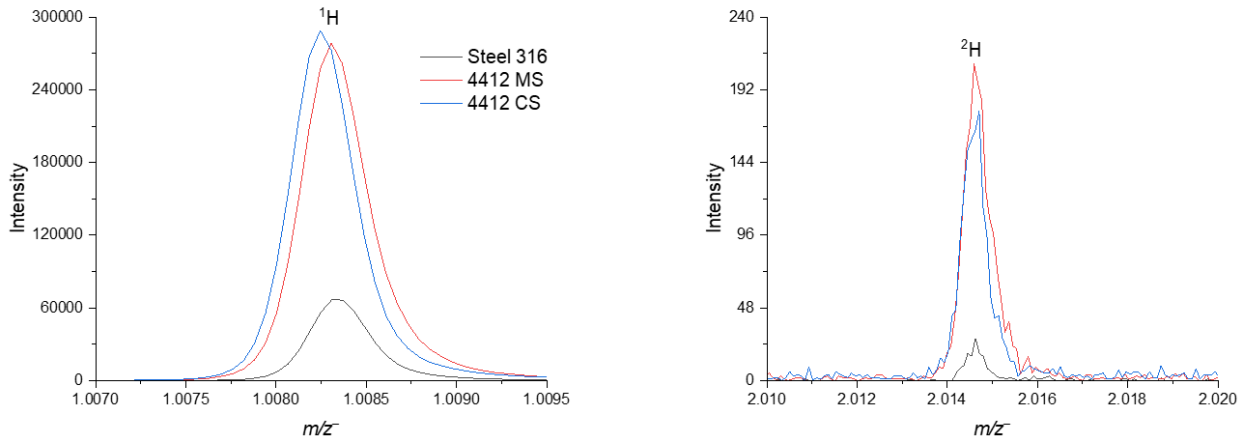

Figure 7: ToF-SIMS negative polarity identifies protium (^{1}H) and deuterium (^{2}H) within the spectra. BFB samples show much higher levels of both protium and deuterium than an unirradiated 316 stainless steel sample (though not from same heat of BFB material).

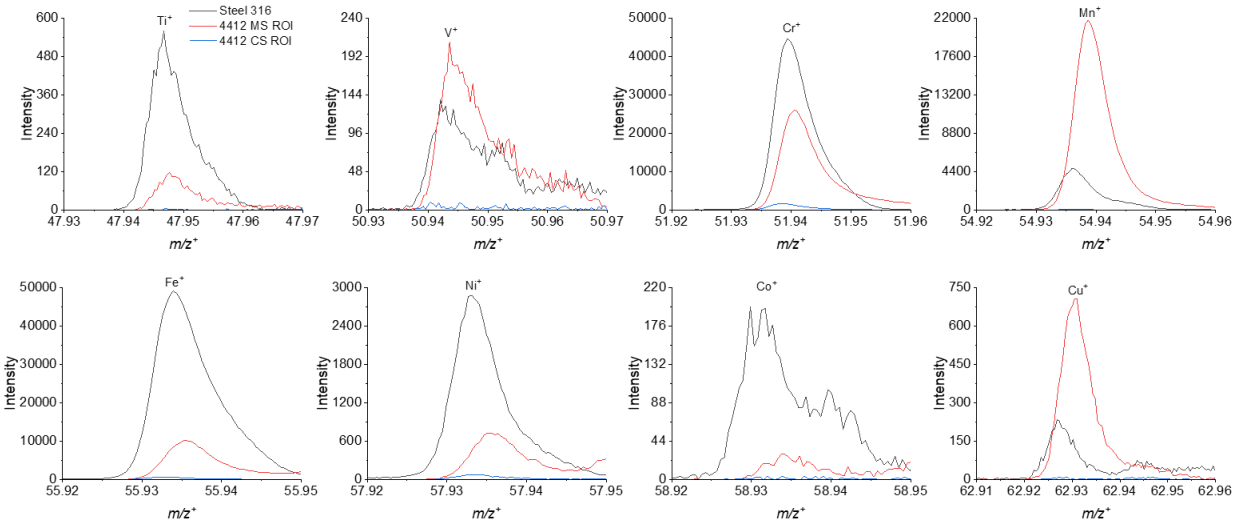

Figure 8: Positive polarity shows peak intensity of possible transmuted elements increases; however, small liftout sample size may attribute error such as the large measured-Mn content in the MS sample, which is likely not real.

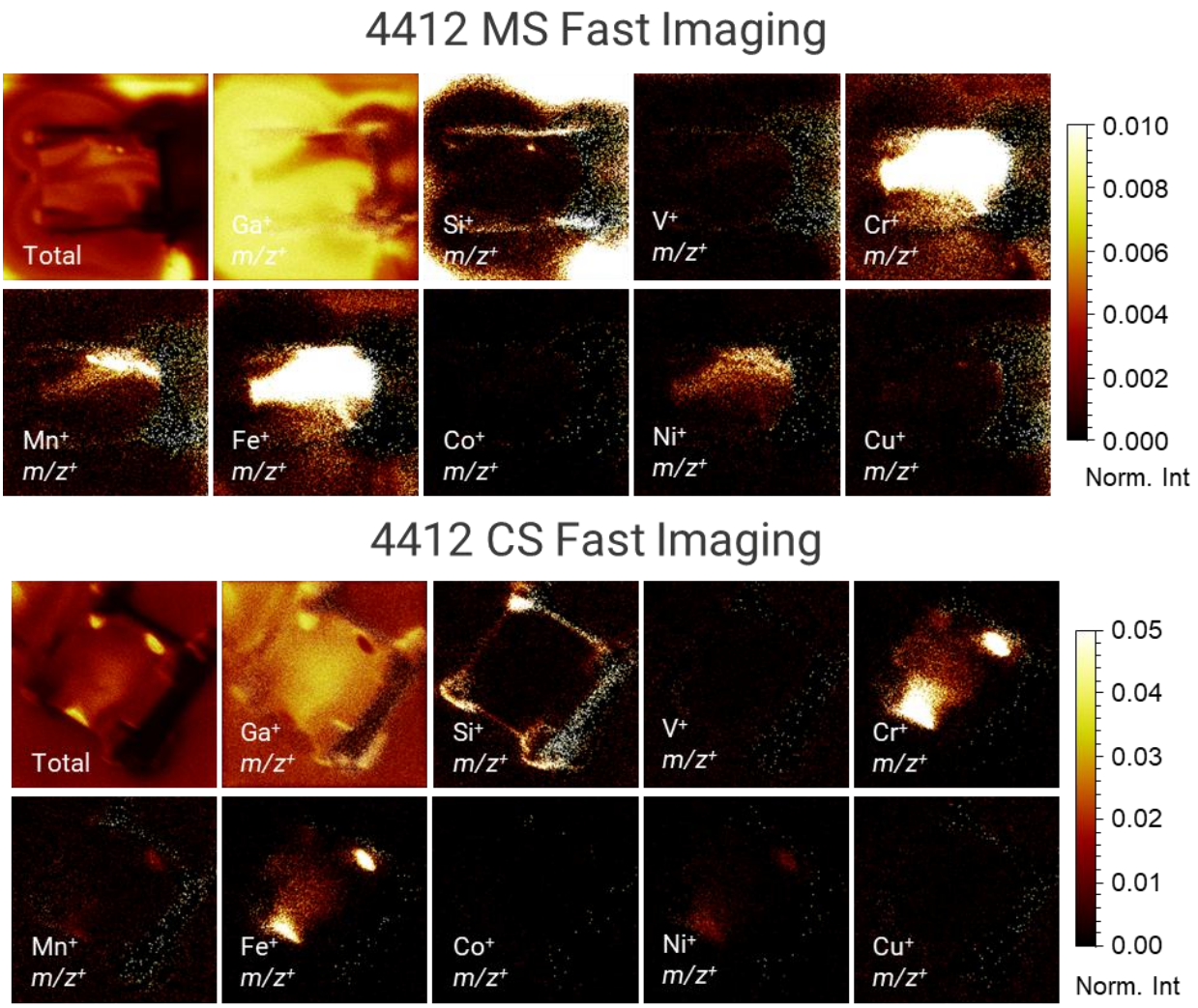

Figure 9: High resolution imaging ToF-SIMS shows spatial distribution shows metal elements of the BFB in select areas. Grain boundaries in samples show no clear difference from the bulk.

3.3 Isotopic measurement comparison with atom probe tomography

Atom probe tomography performs well to quantify and map the spatial distribution of metallic elements as performed previously as part of this task [3, 4]. However, we did not look to use APT for analyzing isotopic hydrogen due to the high background concentration. Further analysis shown in Figure 10 and Table 3 identifies the presence of hydrogen in the samples that is not from the background hydrogen from the chamber. The m/z^+ of 3 Da peak is only from a single tritium ion (T) or a molecular ion of protium and deuterium (HD), with the latter being more likely due to the short half-life of tritium and the calculated relative abundance compared to deuterium. This analysis also shows that the 3 Da peak is highest in the MS and BS sections of the 4412 BFB. However, just as in the ToF-SIMS analysis, this difference is likely quite small and could be non-statistically significant. More analysis by APT and ToF-SIMS is necessary to weed out artefacts. For ToF-SIMS, it is performing depth profiling analysis on larger samples, and for APT, cryogenic FIB combined with cryogenic transfer is necessary to identify and semi-quantify hydrogen isotopes beyond the background level [17].

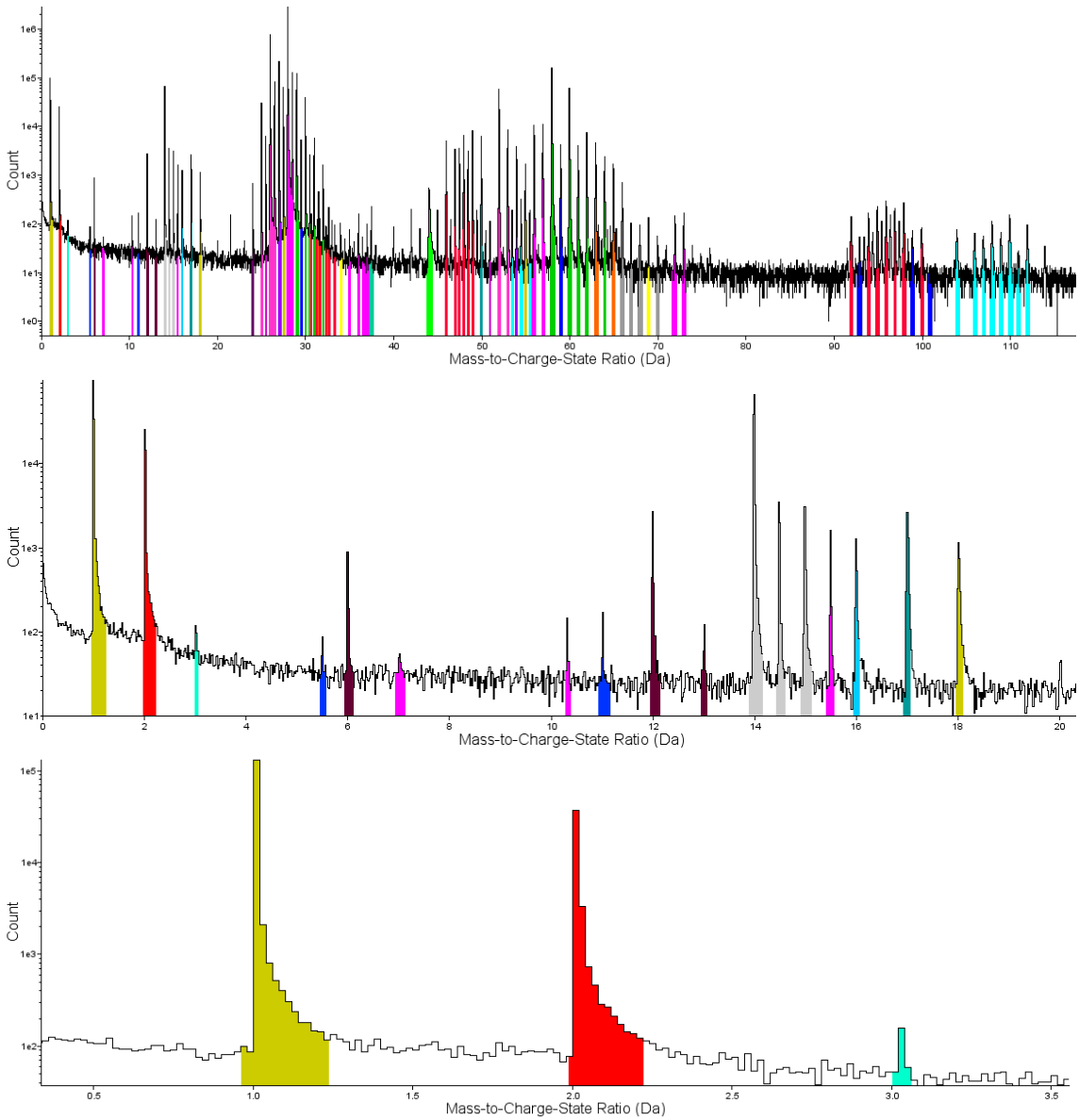

Figure 10: Mass/charge spectrum of a reconstruction of a tip from 4412-CS. The spectrum includes peaks at 1, 2, and 3 Da. Even unirradiated materials contain peaks at 1 and 2 Da due to background hydrogen from the chamber as H and H_2 peaks. However, the peak at 3 Da is likely a result of both an H-D molecule or a singular T ion. Thus, the 2 Da peak likely also contains some D ions.

Table 3: Average ion fraction of each of 1, 2, and 3 Da peaks for each section from both bolts

	Ion fraction					
	4412 CS	**4412 MS**	**4412 BS**	**4416 CS**	**4416 MS**	**4416 BS**
1 Da	0.011374	0.015716	0.019466	0.020461	0.011106	0.01645
2 Da	0.002892	0.005155	0.005282	0.004692	0.00372	0.003609
3 Da	*1.24E-05*	*1.74E-05*	*1.69E-05*	*1.55E-05*	*2.37E-05*	*6.67E-06*

4. Summary and Recommendations

In this report, we present our latest study in FY25 on microstructural and mass spectrum characterizations of the gradients of transmutation gas concentration and cavity density and size along the length of the high dose BFBs. The main findings are summarized as follows:

1. The cavity size distribution was quantified along the length of the high dose bolt #4412 using under-focus transmission electron microscopy. The bolt head section (CS) had a high number density of nanocavities with an average radius of 1.9 nm and a number density of 4.4×10^{22} m^{-3}. The bolt mid-shank (MS) and bolt thread (BS) sections had larger cavities and a lower number density, with the BS section having a clear bimodal distribution. The MS section had an average cavity radius of 3.4 nm and a number density of 4.7×10^{21} m^{-3}. The BS section had an average cavity radius of 4.1 nm and a number density of 5.4×10^{21} m^{-3}, but the distribution of cavities was centered around radii of 2.5 nm and 5 nm. This gradient is consistent with the bolt head having less hydrogen [13] and being at a lower temperature than the bolt shank and thread.
2. Hydrogen isotopes protium and deuterium were detected by ToF-SIMS in the high dose BFB #4412. The results did not show a clear statistically significant difference between sections of the bolt. However, the data were collected on relatively small liftouts and so further analysis by different ToF-SIMS techniques and on larger samples should help identify any gradients in the hydrogen and helium isotope concentrations. The presence of non-background hydrogen was also confirmed by APT as a peak at 3 Da was also identified in every sample from both bolts – a peak that is not present in unirradiated stainless steels.
3. Lessons were learned on the difficulty of measuring hydrogen (and helium) isotopes. The FIB/SEM work requires precision and production of large samples for ToF-SIMS is necessary to remove artefacts from sample analysis – due to hydrocarbon interference. In addition, changing the data collection method such as through the CsM^+ is needed to collect concentration data for inert gases such as helium. Detection of hydrogen isotopes by APT is also possible; however, sample preparation and transfer need to be conducted at cryogenic temperatures in ultrahigh vacuum to limit hydrogen mobility. These lessons will be applied to future work on these and other materials, including the bolt head/shank surface oxide.

5. REFERENCES

1. *Stress Corrosion Cracking in Light Water Reactors: Good Practices and Lessons Learned*. 2011, Vienna: INTERNATIONAL ATOMIC ENERGY AGENCY.
2. Chen, X., et al., *Post-Irradiation Examination of High Fluence Baffle-Former Bolts Retrieved from a Westinghouse Two-Loop Downflow Type PWR, ORNL/TM-2019/1251*. 2019.
3. Lach, T.G., X. Chen, and T.M. Rosseel, *Microstructural Characterization of the Second High Fluence Baffle-Former Bolt Retrieved from a Westinghouse Two-loop Downflow Type PWR, ORNL/TM-2022/2668*. 2022.
4. Lach, T.G., M.N. Gussev, and X.F. Chen, *Microstructural Characterizations of Two High Fluence Baffle-Former Bolts Retrieved from a Westinghouse Two-Loop Downflow Type PWR, ORNL/TM-2023-3078*. 2023.
5. Lach, T.G., M.N. Gussev, and X.F. Chen, *In-service Oxidation and IASCC in High Fluence Baffle-Former Bolts Retrieved from a Westinghouse PWR, ORNL/SPR-2024/3523*. 2024.
6. Chen, X. and M.A. Sokolov, *Fracture Toughness and Fatigue Crack Growth Rate Testing of Baffle-Former Bolts Harvested from a Westinghouse Two-Loop Downflow Type PWR, ORNL/TM-2021/2264*. 2021.
7. Lach, T.G., M.N. Gussev, and X. Chen, *In-service corrosion and grain boundary oxidation in neutron-irradiated 316 stainless steel baffle-former bolts.* Corrosion Science, 2025. **255**: p. 113106.
8. Lach, T.G., M.N. Gussev, and X. Chen, *Complexity of segregation behavior at localized deformation sites formed while in service in a 316 stainless steel baffle-former bolt.* Scripta Materialia, 2025. **255**: p. 116371.
9. X. (Frank) Chen, K.J.L., M.A. Sokolov, M.A. Burke, M.N. Gussev, S.R. Clark, *Specimen Fabrication from Two High Fluence Ginna Baffle Bolts, ORNL/TM-2017/455*. 2017.
10. Lach, T.G. and X. Chen, *Post Irradiation Examination of Pressurized Water Reactor Stainless Steel Internal Components*, in *ASME 2023 Pressure Vessels & Piping Conference, PVP2023*. p. 107347.
11. Chopra, O.K., *Degradation of LWR Core Internal Materials Due to Neutron Irradiation (NUREG/CR-7027)*. 2010.
12. Tang, H.T., *Materials Reliability Program Determination of Operating Parameters of Extracted Bolts (MRP-52)*. 2001: EPRI Technical Report 1003076.
13. Edwards, D.J., et al., *Influence of irradiation temperature and dose gradients on the microstructural evolution in neutron-irradiated 316SS.* Journal of Nuclear Materials, 2003. **317**(1): p. 32-45.
14. Leonard, K.J., M.A. Sokolov, and M.N. Gussev, *Post-Service Examination of PWR Baffle Bolts, Part I. Examination and Test Plan, ORNL/LTR-2015/193*. 2015: United States.
15. Jia, F., X. Zhao, and Y. Zhao, *Advancements in ToF-SIMS imaging for life sciences.* Frontiers in Chemistry, 2023. **Volume 11 - 2023**.
16. Ickes, M.R., et al., *Irradiation-assisted stress corrosion cracking of Type 347 and Type 316 steels irradiated in commercial pressurized water reactors.* Journal of Nuclear Materials, 2020. **536**: p. 152182.
17. Vukkum, V.B., et al., *Insights from quasi-in situ cryogenic-transfer atom probe tomography for analyzing hydrogen diffusion in metallic alloys.* npj Materials Degradation, 2025. **9**(1): p. 85.